Editors' Suggestion | Featured in Physics

# Coexistence of Bloch and Néel walls in a collinear antiferromagnet

M. S. Wörnle,[1,2,*] P. Welter,[1,*] M. Giraldo,[3,*] T. Lottermoser,[3] M. Fiebig,[3,†] P. Gambardella,[2,‡] and C. L. Degen[1,§]

[1]*Department of Physics, ETH Zurich, Otto-Stern-Weg 1, 8093 Zurich, Switzerland*

[2]*Department of Materials, ETH Zurich, Honggerbergring 64, 8093 Zurich, Switzerland*

[3]*Department of Materials, ETH Zurich, Vladimir-Prelog-Weg 4, 8093 Zurich, Switzerland*

(Received 28 August 2020; revised 28 December 2020; accepted 1 February 2021; published 17 March 2021)

We resolve the domain-wall structure of the model antiferromagnet $Cr_2O_3$ using nanoscale scanning diamond magnetometry and second-harmonic-generation microscopy. We find that the 180° domain walls are predominantly Bloch-like, and can coexist with Néel walls in crystals with significant in-plane anisotropy. In the latter case, Néel walls that run perpendicular to a magnetic easy axis acquire a well-defined chirality. We further report quantitative measurement of the domain-wall width and surface magnetization. Our results provide fundamental input and an experimental methodology for the understanding of domain walls in pure, intrinsic antiferromagnets, which is relevant to achieve electrical control of domain-wall motion in antiferromagnetic compounds.

DOI: 10.1103/PhysRevB.103.094426

## I. INTRODUCTION

One of the great unknowns of antiferromagnetism is the domain wall that separates regions with different orientations of the magnetic order parameter. The domain-wall structure influences the thermal stability [1], exchange bias [2], and magnetoresistance [3,4] of antiferromagnets. Furthermore, the type of domain wall, Bloch or Néel, determines their response to current-induced spin torques [5–8], which is of relevance for emerging applications in spintronics of both intrinsic [9–11] and synthetic [12–15] antiferromagnets.

Unlike for ferromagnets [16], the internal structure of the domain walls in antiferromagnets is not generally known. Whereas the antiferromagnetic domain pattern has been imaged for a number of materials including intrinsic antiferromagnets, multiferroics, and magnetically coupled thin films [17–19], these studies generally do not consider the detailed internal domain-wall structure. Exceptions include a few systems where antiferromagnetic order is accompanied by strain [20] or defects [21], monolayer-thin films [22], and synthetic antiferromagnets [13]. By contrast, studies for bulk, intrinsic antiferromagnets still need to be reported. Theoretical analysis suggests that, in the absence of in-plane magnetic anisotropy or a Dzyaloshinskii-Moriya interaction (DMI), no preference is expressed for either Bloch or Néel walls [23–27]. The limited experimental knowledge about antiferromagnetic domain walls is due to a lack of techniques capable of spatially resolving the internal wall structure.

In this paper, we use nanoscale scanning diamond magnetometry (NSDM) to investigate the spin structure of the pure intrinsic antiferromagnet $Cr_2O_3$. NSDM microscopy is an emerging quantum technique for the imaging of weak magnetic fields with nanometer spatial resolution (Fig. 2), with remarkable progress on antiferromagnets [4,28,29], multiferroics [30], and helimagnets [31]. Here, we extend NSDM to the imaging of antiferromagnetic 180° domain-wall structures. We obtain quantitative information about the domain-wall width, chirality, and surface magnetization, and connect it to a model of interplaying demagnetizing and anisotropy energies. We find that both Bloch and Néel walls can be present. Our work extends the knowledge about antiferromagnetic domain-wall structure to the most basic class of intrinsic, bulk antiferromagnets.

## II. ONE-DIMENSIONAL MODEL OF ANTIFERROMAGNETIC DOMAIN WALLS

In order to motivate and explain our experimental observations, we briefly review the conventional model for static one-dimensional (1D) domain walls [23,24] and extend it to collinear antiferromagnets. We consider a 180° domain wall, as it occurs in, for example, $Cr_2O_3$, $\alpha$-$Fe_2O_3$, or CuMnAs. The domain wall separates two regions with magnetic order parameters pointing up ($x < 0$) and down ($x > 0$), as shown schematically in Fig. 1. The key parameters of such a domain wall are the wall width $\Delta$ and the twist angle $\chi$ between the wall magnetization and the $x$ axis. Using this notation, Bloch walls correspond to $\chi = \pm\pi/2$ and Néel walls to $\chi = 0$ ($\pi$) for walls with right (left) chirality. $\Delta$ and $\chi$ are determined by the interplay between exchange and anisotropy energies, and further modified by the demagnetizing field and DMI, if present. Considering only the first two contributions, the local domain-wall energy density in the continuum limit reads

$$e = A\left[\left(\frac{\partial\theta}{\partial x}\right)^2 + \sin^2\theta\left(\frac{\partial\phi}{\partial x}\right)^2\right] + K\sin^2\theta, \qquad (1)$$

*These authors contributed equally to this work.
†manfred.fiebig@mat.ethz.ch
‡pietro.gambardella@mat.ethz.ch
§degenc@ethz.ch

 

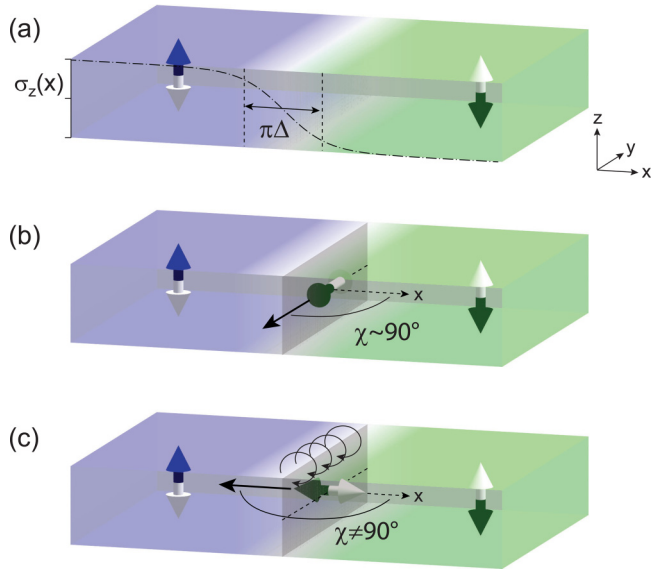


FIG. 1. One-dimensional model for an antiferromagnetic 180° domain wall. (a) Sketch of the domain wall separating regions (purple, green) of opposite order parameter. The dashed-dotted line describes the wall profile as given by Eq. (3c). (b) The presence of a residual demagnetizing field favors the formation of Bloch walls ($\chi = \pm\pi/2$). (c) For sufficiently large in-plane anisotropy in a direction orthogonal to the wall, the formation of a Néel wall ($\chi = 0, \pi$) or mixed Néel-Bloch wall is favored. Curled arrows indicate the demagnetizing field arising from moments crossing the domain wall perpendicularly.

where $A$ is the exchange stiffness, $K$ is the uniaxial anisotropy constant, and $(\theta, \phi)$ are the polar coordinates of the order parameter defined relative to the $z$ axis shown in Fig. 1. The static equilibrium solution that minimizes the total wall energy and satisfies the boundary conditions $\theta(\pm\infty) = (0, \pi)$ is given by

$$\phi(x) = \chi = \text{const}, \tag{2a}$$

$$\theta(x) = \pm 2 \arctan\left[\exp\left(x/\Delta\right)\right], \tag{2b}$$

where $\Delta = \Delta_0 := \sqrt{A/K}$ is the domain-wall width [23,25,26]. The Cartesian coordinates of the order parameter can be easily derived from Eq. (2). For a layered antiferromagnet such as $Cr_2O_3$, it is convenient to express $\theta(x)$ and $\phi(x)$ in terms of the intrinsic surface magnetization $\vec{\sigma}(x)$,

$$\sigma_x(x) = \sigma_z^0 \left[\cosh\left(\frac{x - x_0}{\Delta}\right)\right]^{-1} \cos\chi, \tag{3a}$$

$$\sigma_y(x) = \sigma_z^0 \left[\cosh\left(\frac{x - x_0}{\Delta}\right)\right]^{-1} \sin\chi, \tag{3b}$$

$$\sigma_z(x) = \sigma_z^0 \tanh\left(\frac{x - x_0}{\Delta}\right), \tag{3c}$$

where we assume a domain wall centered at $x = x_0$. The profile of $\sigma_z(x)$ is shown by a dashed-dotted curve in Fig. 1(a). The total energy per unit area of the wall $\epsilon_0$ is given by $\epsilon_0 = 4\sqrt{AK}$.

We stress that, up to this point, the twist angle $\chi$ is arbitrary and independent of $x$. In other words, for an antiferromagnetic system governed solely by exchange and anisotropy energies, Néel and Bloch domain walls (or any combination of the two) are degenerate in energy.

To understand the preference for one type of wall over the other, we next consider the effects of a demagnetizing field $\mu_0 M$ and of an in-plane magnetic anisotropy energy density $K_{\text{ip}}$. We note that, although the volume magnetization $M$ in an antiferromagnet is zero, a finite demagnetizing field still persists when $\phi \neq \pm\pi/2$ due to the net magnetic moment of the domain wall [25,32]. Keeping in mind these additional contributions, the domain-wall energy per unit area changes to [23]

$$\epsilon = \epsilon_0 + \mu_0 M^2 \Delta_0 \cos^2\chi + 2K_{\text{ip}}\Delta_0 \sin^2(\chi - \psi_{\text{ip}}), \tag{4}$$

where the in-plane easy axis is defined by the angle $\psi_{\text{ip}}$ relative to the $x$ axis. According to Eq. (4), the residual demagnetizing field favors the formation of Bloch walls over Néel walls [Fig. 1(b)]. On the other hand, the in-plane anisotropy forces the magnetic moments to cant along the in-plane easy axis, leading to a competition between demagnetizing and anisotropy energies. For a sufficiently large in-plane anisotropy $2K_{\text{ip}} > \mu_0 M^2$ favoring the $x$ direction ($\psi_{\text{ip}} = 0$), we thus expect a Néel-type or a mixed Néel/Bloch-type domain wall [Fig. 1(c)].

The presence of a residual demagnetizing field and of in-plane anisotropy also leads to a modification of the domain-wall width:

$$\Delta = \Delta_0 \left[1 - \frac{\mu_0 M^2}{4K}\cos^2\chi - \frac{K_{\text{ip}}}{2K}\sin^2(\chi - \psi_{\text{ip}})\right]. \tag{5}$$

In particular, Eq. (5) predicts that the width of a Néel wall is reduced with respect to a Bloch wall, with a ratio given by

$$\frac{\Delta_{\text{Néel}}}{\Delta_{\text{Bloch}}} = 1 - \frac{\mu_0 M^2}{4K}, \tag{6}$$

where $M$ is approximately given by the magnetization of the polarized surface layer.

In addition to these interactions, the DMI can further lead to a preference for Néel-type domain walls when the Dzyaloshinskii vector runs parallel to the domain-wall direction (the $y$ axis, Fig. 1) [23,24,33]. Although the DMI is zero in bulk monodomain $Cr_2O_3$ for symmetry reasons [34], the formation of two magnetic domains with an order parameter along $\pm z$ breaks the inversion symmetry between two adjacent spins along $x$. Such a symmetry breaking might allow for a finite DMI or higher-order chiral interactions to emerge in proximity of the domain walls in $Cr_2O_3$ [35]. If such local chiral interactions are larger than or comparable to the demagnetizing energy, the domain walls will be of either Néel or intermediate Bloch-Néel type with a unique chirality. The results presented in our study provide experimental support to this hypothesis.

## III. MATERIALS AND METHODS

We investigate the domain-wall structure and chirality in the prototypical 180° antiferromagnet $Cr_2O_3$. $Cr_2O_3$ is an antiferromagnetic insulator consisting of a hexagonal close packed array of $O^{2-}$ anions with 2/3 of the octahedral holes occupied by $Cr^{3+}$ [36] [Fig. 2(a)]. Below $T_N = 307.6$ K,

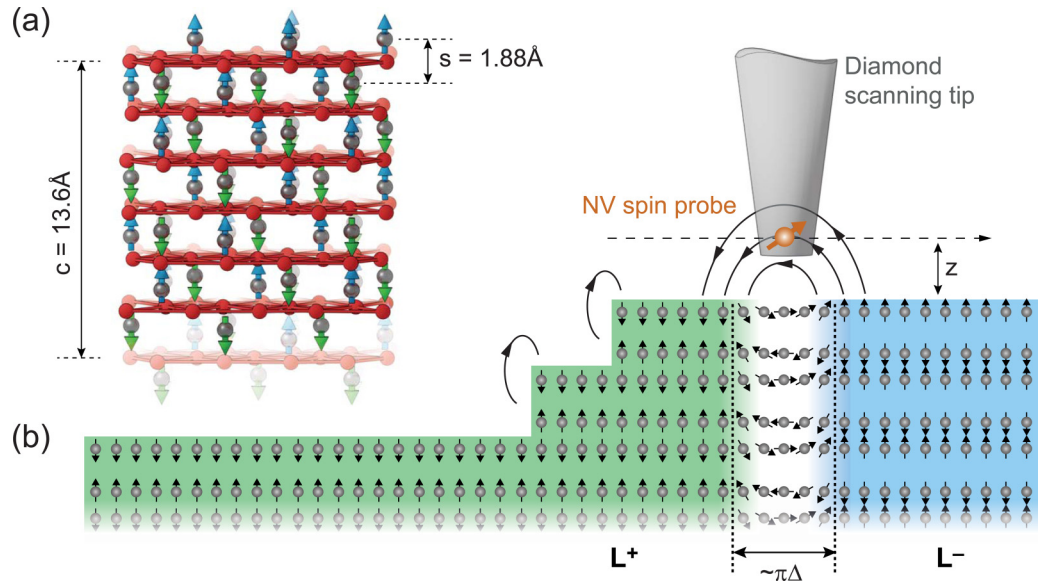


FIG. 2. $Cr_2O_3$ crystal structure and experimental arrangement. (a) Side view of the hexagonal unit cell. Blue and green arrows symbolize $Cr^{3+}$ moments of opposite magnetic polarization, and red atoms are $O^{2-}$ ions. (b) Lateral cut through the *c*-oriented $Cr_2O_3$ sample surface. Strong magnetic stray fields (black field lines) are expected at antiferromagnetic domain walls and weak fields at monolayer topographic steps. Blue and green shading indicate regions of opposite order parameter $L^+$ and $L^-$, defined by the orientation (up or down) of the topmost $Cr^{3+}$ atom in the unit cell [36]. The regions are separated by a domain wall (white) of approximate width $\pi\,\Delta$. The diamond scanning tip and NV center are shown in gray and orange, respectively.

$Cr_2O_3$ forms an antiferromagnetically ordered phase, where the $Cr^{3+}$ ions organize in alternating layers of opposite magnetic polarization [green and blue spins in Fig. 2(a)]. Because of its fundamental role in antiferromagnetism, $Cr_2O_3$ has served as a model system for uniaxial antiferromagnetic order [34,37,38], magnetoelectric coupling [39–41], and electrically controlled exchange bias [42,43]. More recently, $Cr_2O_3$ has attracted attention as a candidate material for antiferromagnetic magnetoelectric random access memories [28], spin colossal magnetoresistance [44], and as a generator of sub-THz spin currents [45]. Although the domain wall plays a critical role in many of these phenomena, the spin structure is unknown beyond initial theoretical work [46], presenting an important experimental test case.

We investigate the $Cr_2O_3$ domain texture of three bulk single crystals. Samples A and B are grown by the Verneuil method and polished to a surface roughness of 1–3 nm rms. Sample C is a flux-grown platelet with an as-grown surface. In a previous study [47], we found that the spin-flop transition—normally requiring a magnetic field of 5.8 T [36]—occurs spontaneously at 150 K in sample C, pointing to an unusually strong in-plane anisotropy. In addition, this sample has a lower Néel temperature ($T_N = 304.6$ K), probably due to strain or oxygen deficiency. We create antiferromagnetic domains by repeatedly cooling samples through the transition temperature $T_N$ using magnetoelectric poling [48] or until a multidomain state spontaneously forms. Further details about the samples are given in the Supplemental Material [49].

We use a combination of optical second-harmonic-generation (SHG) microscopy and NSDM to locate the antiferromagnetic domains and measure the domain-wall profile. SHG is a nonlinear optical method capable of resolving the global 180° domain pattern, yet has a diffraction-limited spatial resolution and is not sensitive to the absolute sign of the order parameter [49,50]. To map the stray field distribution, we scan a diamond tip with a nitrogen-vacancy (NV) center (orange arrow) at a constant height ($z = 60$–$70$ nm) above the sample surface [Fig. 2(b)]. The NV spin detects the component of the stray magnetic field $B_{NV}$ parallel to its internal anisotropy axis (here, 55° off the surface normal [49]). The experiments are performed under ambient conditions at a temperature of 295 K.

## IV. EXPERIMENTAL RESULTS

### A. Domain states

Figure 3(a) shows a laser-optical second-harmonic-generation (SHG) [47] micrograph of the global domain pattern. We observe that the domains in the bulk $Cr_2O_3$ crystals are large, typically in the range of hundreds of micrometers, and stable below $T_N$, in agreement with earlier studies [50]. We find no correlation between the domain pattern and the in-plane crystal axes [Fig. 3(a)], indicating that the domain-wall location is set by the local defect or strain distribution or is completely random.

Once the domains are localized, we acquire high-resolution magnetic imaging scans along the domain walls using NSDM microscopy [Fig. 3(b)]. The domain wall appears as a narrow track of a strong magnetic stray field in the magnetometry image; this strong field is due to the 180° reversal of uncompensated moments near the sample surface [see Fig. 2(b)]. Fainter features within the domains reflect residual stray fields associated with surface topography [51]. We do not observe

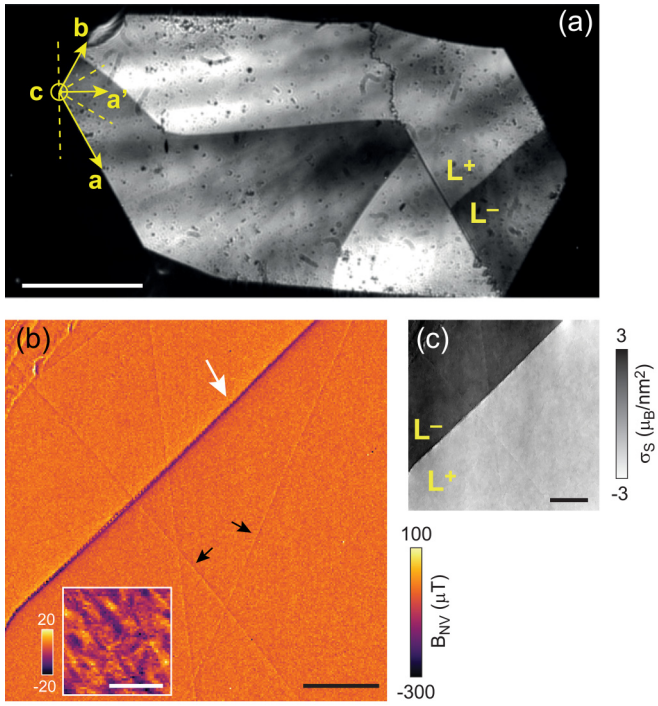


FIG. 3. Antiferromagnetic domain pattern in $c$-oriented $Cr_2O_3$. (a) SHG image revealing bright and dark domains of opposite order parameter in sample C; corresponding images for samples A and B are given in Figs. S1 and S2 in the Supplemental Material [49]. The order parameter ($L^+$ and $L^-$) is assigned based on the magnetization map in (c). The image is acquired with right-handed circularly polarized illumination. The twofold axes $a$, $a'$, and $b$ (yellow vectors), determined by x-ray crystallography, coincide with the in-plane magnetic easy axes of the spin-flop phase. Dashed lines indicate the in-plane magnetic hard axes. Scale bar: 500 $\mu$m.(b) Magnetometry image of the stray field above a domain wall (white arrow) in sample A. Fainter features are due to surface topography, such as scratch marks from sample polishing (black arrows). The inset shows a high-sensitivity scan above a uniform domain on sample B, revealing weak stray fields due to surface roughness [49]. Dwell time per pixel is 1.5 s and total acquisition time is 26 h. (c) Surface magnetization $\sigma_z$ reconstructed from the stray field map of (b), given in units of Bohr magnetons ($\mu_B$) per nm$^2$. Scale bars for (b) and (c): 2 $\mu$m.

any correlation between the domain-wall location and the sample structure, suggesting that there are no surface-induced pinning effects. Further, when cycling the sample through the transition temperature $T_N$, domain walls usually form in random locations of the sample with no correlation between consecutive warming-cooling cycles.

To retrieve the absolute sign of the order parameter we reconstruct [49] the two-dimensional (2D) surface magnetization $\sigma_z$ from the stray field map of Fig. 3(b), shown in Fig. 3(c). Here, a positive sign of $\sigma_z$ (dark contrast) reflects a positive $Cr^{3+}$ surface magnetization and order parameter $L^-$ (vice versa for $L^+$). We find that the correlation between SHG contrast and surface magnetization is maintained for all domain walls on all samples (Figs. S1 and S2 in the Supplemental Material [49]). Combined with the absence of strong magnetic features in the interior of domains, these findings directly confirm that the magnetic polarization of $Cr_2O_3$ is robust against surface roughness [29,43], and that $Cr_2O_3$ always terminates with the same $Cr^{3+}$ surface magnetization for a given sign of the order parameter $L$.

### B. Domain-wall cross section

To investigate the internal structure of a domain wall, we acquire a large number of magnetometry images along the domain wall and analyze the magnitude and spatial profile of the stray field [52,53]. We then compare the magnetic field along the cross section with the expected stray field from the static solution of the one-dimensional domain-wall model [Eq. (3)] and compute the magnetic stray field using forward propagation [49]. By fitting the computed stray field to the experimental cross section, we obtain quantitative estimates for the surface magnetization $\sigma_z^0$, domain-wall width $\Delta$, and twist angle $\chi$. Figures 4(a) and 4(b) show an exemplary line scan across a domain wall of sample C together with the least-squares fit. To build statistics and avoid possible cross-correlation between the fit parameters, we analyze about $10^3$ line scans for each sample and validate results by a secondary data analysis (Figs. S3 and S4 in the Supplemental Material [49]). To exclude long-term drifts, we acquire scans along a domain wall in random order and find no temporal correlations as we proceed with the scanning.

### C. Surface magnetization

Figure 4(c) reports quantitative measurements of the surface magnetization $\sigma_z^0$. We find a narrow distribution of $\sigma_z^0$ values ranging from $1.6(2)\mu_B/nm^2$ in sample C to $2.3(2)\mu_B/nm^2$ in sample A. These values are only 15%–21% of the the theoretical $\sigma_z^0$ for a perfectly ordered $Cr^{3+}$ crystal, which is $\sigma_z^0(0) = 10.9\mu_B/nm^2$ for the surface termination shown in Fig. 3(a) at zero temperature [49]. The low $\sigma_z^0$ is partially explained by the decay of magnetic order close to $T_N$, and is more pronounced for sample C due to the lower $T_N$. According to Ref. [29], the surface magnetization close to $T_N$ is approximately given by $\sigma_z^0(T) = \sigma_z^0(0)[1 - (T/T_N)]^{0.35}$, which gives $\sigma_z^0(T)/\sigma_z^0(0) \sim 30\%$ at $T = 295$ K. Since low values for $\sigma_z^0$ have also been reported by other experimental studies [29,54], and since we observe a narrow distribution of $\sigma_z^0$ that is uniform across the sample surface, we believe that the reduced $\sigma_z^0$ is a general and unexplained property of $Cr_2O_3$. We hypothesize that the reduced surface moment density may be due to disorder within the exposed layer of terminating $Cr^{3+}$ ions [see Fig. 2(a)].

### D. Domain-wall chirality and width

Figures 5(a)–5(c) plot the fit results for the domain-wall width $\Delta$ and angle $\chi$ obtained from the extensive data sets recorded on samples A–C. Each plotted ($\chi$, $\Delta$) pair represents a $\sim 4 \times 4$ $\mu$m$^2$ magnetometry scan, and color coding reflects the propagation direction of the domain wall. For samples A and B we find all domain walls to be predominantly Bloch-like, indicated by a $\chi$ angle close to 90° [Figs. 5(a) and 5(b)]. The domain-wall widths are not identical, but of similar magnitude $\Delta \sim 40$ nm, and well within the range of 20–80 nm predicted by theory [46]. Clearly, there is no correlation

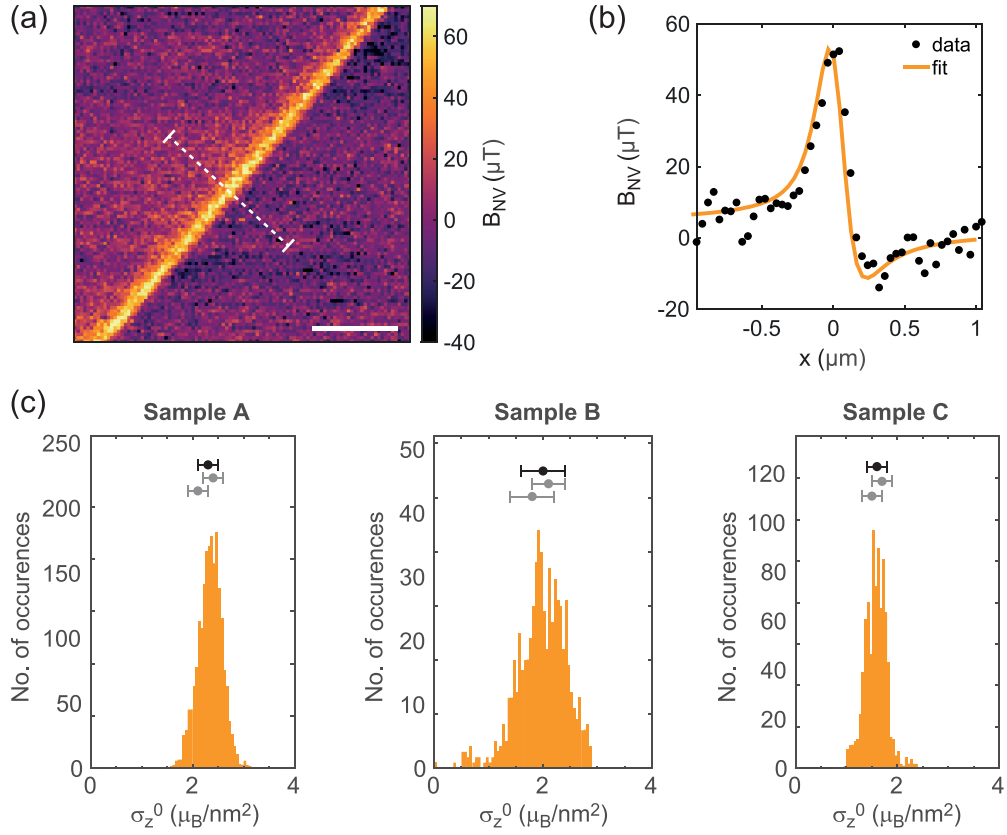


FIG. 4. Quantitative measurement of domain-wall structure and surface magnetization. (a) Two-dimensional magnetometry scan of a domain wall in sample C. Scale bar: 1 $\mu$m. (b) Cross section along the white dashed line in (a), showing the stray field $B_{\mathrm{NV}}(x)$ as a function of the relative distance $x$ to the domain wall. Dots are the experimental data and the solid line is a fit to the domain-wall model given by Eq. (3). Free fit parameters are the surface magnetization $\sigma_z^0$, the domain-wall width $\Delta$, and the angle $\chi$ [49]. (c) Histograms of $\sigma_z^0$ obtained from many line scan fits. Mean and standard deviation (s.d.) are included above the histograms as black dots with horizontal error bars ($\pm 1$ s.d.). Light gray bars reflect the $\sigma_z^0$ values obtained by a secondary analysis (see Supplemental Material [49]; the central bar reflects the step height, and the lower bar reflects the integrated $B_x$ field). The number of line scans per histogram are 2512 for sample A, 726 for sample B, and 1012 for sample C.

between $(\chi, \Delta)$ and the spatial location or propagation direction $\alpha$ of the domain wall [see Figs. 5(d) and 5(e)], indicating that the crystal structure plays no role in domain-wall formation. The consistency of the results from the two samples, which are grown independently by the same technique, confirms that our methods for quantifying the domain-wall structure are robust and reproducible.

Interestingly, sample C—which has an unusually strong in-plane anisotropy [47]—shows a behavior that is distinctly different from samples A and B. Most prominently, we find both Néel and Bloch walls and a pronounced dependence of the twist angle on the wall orientation. For walls that run approximately parallel to one of magnetic hard axes [dashed lines in Figs. 3(a) and 5(d)–5(f)], the domain wall has a distinct left Néel character [blue data points in Fig. 5(c)]. Once the angle $\alpha$ between the propagation direction and the hard axis exceeds about 9°, the wall changes to Bloch type, and becomes similar to samples A and B. In addition, the domain-wall width increases from $\Delta = 42$ nm in the Néel to $\Delta = 65$ nm in the Bloch configuration. The correlation between $(\chi, \Delta)$ and $\alpha$ is not complete, but pervasive, suggesting that a delicate balance of interactions determines the local structure of the wall.

## V. DISCUSSION

The formation of distinct Bloch and Néel walls in $Cr_2O_3$ is intriguing, because in the absence of a demagnetizing field and in-plane anisotropy, the domain-wall energy of a collinear antiferromagnet is independent of the angle $\chi$ [23,25,26,49]. Therefore, no domain-wall type is energetically favored. In $Cr_2O_3$, however, domain walls have a nonvanishing local magnetic moment associated with the spatially inhomogeneous order parameter [25,32], giving rise to a small but nonzero demagnetizing field. We propose that this residual demagnetizing field, which is mostly a bulk effect, is responsible for the observation of Bloch walls in samples A and B, similar to the situation encountered in uniaxial ferromagnets [16].

The preference for Bloch walls is challenged once significant in-plane anisotropy is present (sample C). An in-plane anisotropy favors $Cr^{3+}$ spins aligned with the in-plane easy axis and for a sufficiently strong anisotropy, the domain wall is expected to change from Bloch to Néel (see Sec. II). Due to the threefold crystal symmetry of $Cr_2O_3$, three in-plane easy axes exist [that coincide with the crystal axes $a$, $a'$, and $b$, see Fig. 3(a)] leading to six preferred directions in 60° intervals.

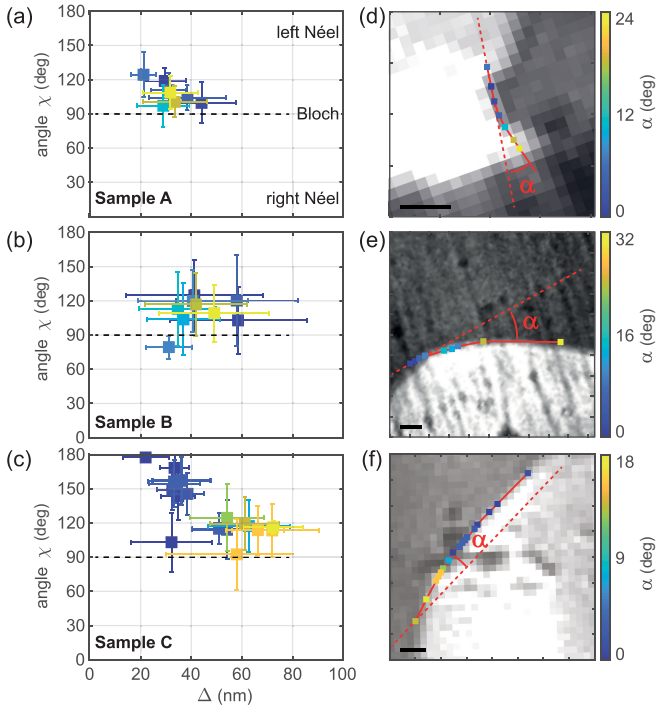


FIG. 5. Observation of Bloch and Néel walls. (a)–(c) Twist angle $\chi$ plotted against the domain-wall width $\Delta$ for samples A–C. Each point represents the data from a two-dimensional magnetometry scan. Error bars ($\pm 1$ s.d.) are obtained by separate fits to each line of the 2D scan and computing the standard deviation (s.d.) of the fit results. Color coding reflects the propagation direction of the domain wall (see right panels). No correlation between chirality and spatial position is evident for samples A and B, whereas a clear correlation is evident for sample C. Mean angle and domain-wall widths are $(\chi, \Delta) = [106(6)^\circ, 34(5)\ \text{nm}]$ for sample A, $[113(11)^\circ, 45(8)\ \text{nm}]$ for sample B, $[143(12)^\circ, 42(6)\ \text{nm}]$ for sample C with $\alpha < 9^\circ$, and $[117(7)^\circ, 65(4)\ \text{nm}]$ for sample C with $\alpha > 9^\circ$; brackets denote standard error. (d)–(f) SHG images of the domain-wall regions analyzed in (a)–(c). Colored squares show the scan locations. $\alpha$ is the angle between the local propagation direction of the domain wall (red solid line) and one of the magnetic hard axes [red dashed line, see Fig. 3(a)]. Scale bars: 25 $\mu$m.

Therefore, the $Cr^{3+}$ spins will tend to align to the nearest preferred easy direction. The alignment is strongest when the domain wall is perpendicular to an easy axis, explaining the appearance of Néel walls near $\alpha \approx 0^\circ$ [blue data points in Fig. 5(c)]. Once $\alpha$ becomes larger, the in-plane anisotropy torque is reduced, and the domain wall eventually changes back to a Bloch type (yellow data points). The critical angle where this change occurs is not well defined, but is roughly $\alpha \approx 9^\circ$. At the same time as the domain-wall type changes from Néel to Bloch, the domain-wall width is expected to increase, in line with our observation [Fig. 5(c)]. Using Eq. (6) and setting $M = s\sigma_z^0$, the one-dimensional model predicts a ratio of domain-wall widths of $\Delta^{\text{Neel}}/\Delta^{\text{Bloch}} = 0.85$ for $Cr_2O_3$, in reasonably agreement with the experimental result of $r = 0.65 \pm 0.10$ [Fig. 5(c)]. The good overall agreement between experiment and theory motivates the conclusion that the nonvanishing magnetic moment and in-plane anisotropy determine the domain-wall structure of $Cr_2O_3$.

A final point that remains to be explained is the preference for left chiral Néel walls in sample C, which is also partially present in samples A and B [Figs. 5(a)–5(c)]. Although the asymmetry is conspicuous, it is not entirely surprising given the complex magnetoelectric properties of $Cr_2O_3$ [48]. Because the orientation of the spins in a left chiral Néel wall is against the stray field produced by the uncompensated magnetization of the topmost surface layers of $Cr_2O_3$ [Fig. 2(b)], the preference for left walls cannot be attributed to a magnetostatic effect, unlike the change of a Bloch wall into a Néel wall observed in the near-surface region of ferromagnets [16]. Future theoretical work shall determine whether a wall-related DMI or higher-order multispin interactions are responsible for the domain-wall chirality (see Sec. II). In a noncentrosymmetric environment, the DMI results in canting of the spins when $L$ has a nonzero in-plane component [34,55], which, unlike in bulk $Cr_2O_3$, may be the case *within* the $Cr_2O_3$ domain wall.

## VI. SUMMARY AND OUTLOOK

In summary, we have resolved the spin structure of 180° domain walls in the prototype uniaxial antiferromagnet $Cr_2O_3$. We propose that the structure of the domain wall is determined by the weak energy scales provided by the nonvanishing magnetization of the wall, the in-plane magnetic anisotropy, and possibly the DMI. Domain walls are Bloch-like in crystals with weak or negligible in-plane magnetic anisotropy, and either Bloch- or Néel-like in the crystal with larger in-plane anisotropy. In the latter case, the domain-wall type turns to Néel if the wall runs orthogonal to an in-plane easy axis, which coincides with the spin direction in the spin-flop phase of $Cr_2O_3$ [36]. In agreement with simple theoretical considerations, the domain-wall width decreases from $\Delta = 65$ nm in the Bloch configuration to $\Delta = 42$ nm in the Néel configuration. Finally, the comparison between SHG and NSDM allows for determining the absolute sign of the order parameter in different domains, which is not possible by optical imaging alone.

Besides its fundamental interest, insight into the domain walls of collinear antiferromagnets is relevant for the development of antiferromagnetic spintronic devices that exploit current-induced domain-wall motion to switch the orientation of the order parameter [6,7]. For example, in antiferromagnetic/heavy-metal bilayers the domain-wall velocity is predicted to be zero for Bloch walls when considering only the dampinglike spin-orbit torque, and nonzero but offset by a threshold current density when including the fieldlike spin-orbit torque [7]. In contrast, a nonzero domain-wall velocity is predicted for Néel walls at any current density (in the absence of pinning), making this type of wall much more efficient for achieving current-induced domain-wall displacements. In our work, we show that the residual demagnetization field in the walls of a collinear antiferromagnet with unixial anisotropy favors the formation of Bloch walls, whereas the presence of in-plane magnetocrystalline anisotropy, likely in combination with chiral spin interactions, favors the formation of Néel walls. Future studies should aim at confirming the presence of a wall-related bulk DMI in $Cr_2O_3$ and determine

whether an additional interfacial DMI can be induced by proximity to a heavy metal such as Pt.

## ACKNOWLEDGMENTS

We acknowledge T. Weber for support with the X-ray platform at the Materials Department of ETH Zurich, and N.A. Spaldin and S. Blügel for insightful discussions. This work was supported by ETH Zurich and the Swiss Competence Centre for Materials Science and Technology (CCMX). C.D. acknowledges support by the Swiss National Science Foundation (SNSF) under Grant No. 200020_175600, by the SNSF under the NCCR QSIT, and by the European Commission under Grant No. 820394 "ASTERIQS." P.G. acknowledges support by the SNSF under Grant No. 200020_172775. M.F. acknowledges support by the SNSF under Grant No. 200021_178825 and FAST, a division of the NCCR MUST, funded by the SNSF. M.S.W. and P.W. built the NSDM setup and performed the NSDM measurements; M.G. prepared the antiferromagnetic domains and performed the SHG and x-ray crystallography measurements; M.S.W. and C.L.D. analyzed the data with help from P.W. and P.G.; M.S.W, M.F. P.G., and C.L.D. cowrote the paper; all authors discussed the results.

[1] O. Shpyrko, E. Isaacs, J. Logan, Y. Feng, G. Aeppli, R. Jaramillo, H. Kim, T. Rosenbaum, P. Zschack, M. Sprung *et al.*, Direct measurement of antiferromagnetic domain fluctuations, Nature (London) **447**, 68 (2007).

[2] F. Radu and H. Zabel, Exchange bias effect of ferro-/antiferromagnetic heterostructures, in *Magnetic Heterostructures* (Springer, Berlin, 2008), pp. 97–184.

[3] R. Jaramillo, T. F. Rosenbaum, E. D. Isaacs, O. G. Shpyrko, P. G. Evans, G. Aeppli, and Z. Cai, Microscopic and Macroscopic Signatures of Antiferromagnetic Domain Walls, Phys. Rev. Lett. **98**, 117206 (2007).

[4] M. Wörnle, P. Welter, Z. Kašpar, K. Olejník, V. Novák, R. Campion, P. Wadley, T. Jungwirth, C. Degen, and P. Gambardella, Current-induced fragmentation of antiferromagnetic domains, arXiv:1912.05287.

[5] K. M. D. Hals, Y. Tserkovnyak, and A. Brataas, Phenomenology of Current-Induced Dynamics in Antiferromagnets, Phys. Rev. Lett. **106**, 107206 (2011).

[6] O. Gomonay, T. Jungwirth, and J. Sinova, High Antiferromagnetic Domain Wall Velocity Induced by Néel Spin-Orbit Torques, Phys. Rev. Lett. **117**, 017202 (2016).

[7] T. Shiino, S.-H. Oh, P. M. Haney, S.-W. Lee, G. Go, B.-G. Park, and K.-J. Lee, Antiferromagnetic Domain Wall Motion Driven by Spin-Orbit Torques, Phys. Rev. Lett. **117**, 087203 (2016).

[8] L. Baldrati, O. Gomonay, A. Ross, M. Filianina, R. Lebrun, R. Ramos, C. Leveille, F. Fuhrmann, T. R. Forrest, F. Maccherozzi, S. Valencia, F. Kronast, E. Saitoh, J. Sinova, and M. Kläui, Mechanism of Néel Order Switching in Antiferromagnetic Thin Films Revealed by Magnetotransport and Direct Imaging, Phys. Rev. Lett. **123**, 177201 (2019).

[9] T. Jungwirth, X. Marti, P. Wadley, and J. Wunderlich, Antiferromagnetic spintronics, Nat. Nanotechnol. **11**, 231 (2016).

[10] V. Baltz, A. Manchon, M. Tsoi, T. Moriyama, T. Ono, and Y. Tserkovnyak, Antiferromagnetic spintronics, Rev. Mod. Phys. **90**, 015005 (2018).

[11] A. Manchon, J. Železný, I. M. Miron, T. Jungwirth, J. Sinova, A. Thiaville, K. Garello, and P. Gambardella, Current-induced spin-orbit torques in ferromagnetic and antiferromagnetic systems, Rev. Mod. Phys. **91**, 035004 (2019).

[12] R. A. Duine, K. J. Lee, S. S. P. Parkin, and M. D. Stiles, Synthetic antiferromagnetic spintronics, Nat. Phys. **14**, 217 (2018).

[13] S.-H. Yang, K.-S. Ryu, and S. Parkin, Domain-wall velocities of up to 750 m/s driven by exchange-coupling torque in synthetic antiferromagnets, Nat. Nanotechnol. **10**, 221 (2015).

[14] Z. Luo, T. P. Dao, A. Hrabec, J. Vijayakumar, A. Kleibert, M. Baumgartner, E. Kirk, J. Cui, T. Savchenko, G. Krishnaswamy, L. J. Heyderman, and P. Gambardella, Chirally coupled nanomagnets, Science **363**, 1435 (2019).

[15] A. Hrabec, Z. Luo, L. J. Heyderman, and P. Gambardella, Synthetic chiral magnets promoted by the Dzyaloshinskii-Moriya interaction, Appl. Phys. Lett. **117**, 130503 (2020).

[16] A. Hubert and R. Schäfer, *Magnetic Domains: The Analysis of Magnetic Microstructures* (Springer, Berlin, 2008).

[17] Y. Geng, H. Das, A. L. Wysocki, X. Wang, S. W. Cheong, M. Mostovoy, C. J. Fennie, and W. Wu, Direct visualization of magnetoelectric domains, Nat. Mater. **13**, 163 (2014).

[18] S. W. Cheong, M. Fiebig, W. Wu, L. Chapon, and V. Kiryukhin, Seeing is believing: Visualization of antiferromagnetic domains, npj Quantum Mater. **5**, 3 (2020).

[19] O. Hellwig, A. Berger, and E. E. Fullerton, Domain Walls in Antiferromagnetically Coupled Multilayer Films, Phys. Rev. Lett. **91**, 197203 (2003).

[20] N. B. Weber, H. Ohldag, H. Gomonaj, and F. U. Hillebrecht, Magnetostrictive Domain Walls in Antiferromagnetic NiO, Phys. Rev. Lett. **91**, 237205 (2003).

[21] R. Ravlić, M. Bode, A. Kubetzka, and R. Wiesendanger, Correlation of dislocation and domain structure of Cr(001) investigated by spin-polarized scanning tunneling microscopy, Phys. Rev. B **67**, 174411 (2003).

[22] M. Bode, E. Vedmedenko, K. Von Bergmann, A. Kubetzka, P. Ferriani, S. Heinze, and R. Wiesendanger, Atomic spin structure of antiferromagnetic domain walls, Nat. Mater. **5**, 477 (2006).

[23] A. Malozemoff and J. Slonczewski, *Magnetic Domain Walls in Bubble Materials: Advances in Materials and Device Research* (Academic, New York, 2016), Vol. 1.

[24] E. M. Gyorgy and F. B. Hagedorn, Analysis of domain-wall motion in canted antiferromagnets, J. Appl. Phys. **39**, 88 (1968).

[25] N. Papanicolaou, Antiferromagnetic domain walls, Phys. Rev. B **51**, 15062 (1995).

[26] C. Mitsumata and A. Sakuma, Generalized model of antiferromagnetic domain wall, IEEE Trans. Magn. **47**, 3501 (2011).

[27] Z. Y. Chen, Z. R. Yan, M. H. Qin, and J.-M. Liu, Landau-Lifshitz-Bloch equation for domain wall motion in antiferromagnets, Phys. Rev. B **99**, 214436 (2019).

[28] T. Kosub, M. Kopte, R. Hühne, P. Appel, B. Shields, P. Maletinsky, R. Hübner, M. O. Liedke, J. Fassbender, and O. G. Schmidt, Purely antiferromagnetic magnetoelectric random access memory, Nat. Commun. **8**, 1 (2017).

[29] P. Appel, B. J. Shields, T. Kosub, N. Hedrich, R. Hubner, J. Fassbender, D. Makarov, and P. Maletinsky, Nanomagnetism of magnetoelectric granular thin-film antiferromagnets, Nano Lett. **19**, 1682 (2019).

[30] I. Gross, W. Akhtar, V. Garcia, L. Martínez, S. Chouaieb, K. Garcia, C. Carrétéro, A. Barthélémy, P. Appel, P. Maletinsky *et al.*, Real-space imaging of non-collinear antiferromagnetic order with a single-spin magnetometer, Nature (London) **549**, 252 (2017).

[31] A. Dussaux, P. Schoenherr, K. Koumpouras, J. Chico, K. Chang, L. Lorenzelli, N. Kanazawa, Y. Tokura, M. Garst, A. Bergman, C. L. Degen, and D. Meier, Local dynamics of topological magnetic defects in the itinerant helimagnet FeGe, Nat. Commun. **7**, 12430 (2016).

[32] E. G. Tveten, T. Müller, J. Linder, and A. Brataas, Intrinsic magnetization of antiferromagnetic textures, Phys. Rev. B **93**, 104408 (2016).

[33] M. Heide, G. Bihlmayer, and S. Blügel, Dzyaloshinskii-Moriya interaction accounting for the orientation of magnetic domains in ultrathin films: Fe/W (110), Phys. Rev. B **78**, 140403(R) (2008).

[34] I. Dzyaloshinsky, A thermodynamic theory of "weak" ferromagnetism of antiferromagnetics, J. Phys. Chem. Solids **4**, 241 (1958).

[35] T. Moriya, Anisotropic superexchange interaction and weak ferromagnetism, Phys. Rev. **120**, 91 (1960).

[36] M. Fiebig, D. Fröhlich, and H. J. Thiele, Determination of spin direction in the spin-flop phase of $Cr_2O_3$, Phys. Rev. B **54**, R12681(R) (1996).

[37] G. T. Rado and V. J. Folen, Magnetoelectric effects in antiferromagnetics, in *Proceedings of the Seventh Conference on Magnetism and Magnetic Materials*, edited by J. A. Osborn (Springer, Boston, 1962), pp. 1126–1132.

[38] B. N. Brockhouse, Antiferromagnetic structure in $Cr_2O_3$, J. Chem. Phys. **21**, 961 (1953).

[39] D. Astrov, Magnetoelectric effect in chromium oxide, J. Exptl. Theoret. Phys. (U.S.S.R.) **40**, 1035 (1961) [Sov. Phys. JETP **13**, 729 (1961)].

[40] T. Martin and J. Anderson, Antiferromagnetic domain switching in $Cr_2O_3$, IEEE Trans. Magn. **2**, 446 (1966).

[41] M. Mostovoy, A. Scaramucci, N. A. Spaldin, and K. T. Delaney, Temperature-Dependent Magnetoelectric Effect from First Principles, Phys. Rev. Lett. **105**, 087202 (2010).

[42] P. Borisov, A. Hochstrat, X. Chen, W. Kleemann, and C. Binek, Magnetoelectric Switching of Exchange Bias, Phys. Rev. Lett. **94**, 117203 (2005).

[43] X. He, Y. Wang, N. Wu, A. N. Caruso, E. Vescovo, K. D. Belashchenko, P. A. Dowben, and C. Binek, Robust isothermal electric control of exchange bias at room temperature, Nat. Mater. **9**, 579 (2010).

[44] Z. Qiu, D. Hou, J. Barker, K. Yamamoto, O. Gomonay, and E. Saitoh, Spin colossal magnetoresistance in an antiferromagnetic insulator, Nat. Mater. **17**, 577 (2018).

[45] J. Li, C. B. Wilson, R. Cheng, M. Lohmann, M. Kavand, W. Yuan, M. Aldosary, N. Agladze, P. Wei, M. S. Sherwin *et al.*, Spin current from sub-terahertz-generated antiferromagnetic magnons, Nature (London) **578**, 70 (2020).

[46] Y. Kota and H. Imamura, Narrowing of antiferromagnetic domain wall in corundum-type $Cr_2O_3$ by lattice strain, Appl. Phys. Express **10**, 013002 (2016).

[47] R. V. Pisarev, M. Fiebig, and D. Fröhlich, Nonlinear optical spectroscopy of magnetoelectric and piezomagnetic crystals, Ferroelectrics **204**, 1 (1997).

[48] B. B. Krichevtsov, V. V. Pavlov, and R. V. Pisarev, Nonreciprocal optical effects in antiferromagnetic $Cr_2O_3$ subjected to electric and magnetic fields, Zh. Eksp. Teor. Fiz. **94**, 284 (1988) [Sov. Phys. JETP **67**, 378 (1988)].

[49] See Supplemental Material at http://link.aps.org/supplemental/10.1103/PhysRevB.103.094426 for Materials and Methods, Data Analysis, and Supplementary Figures, which includes Refs. [48,56–64].

[50] M. Fiebig, D. Fröhlich, G. Sluyterman v. L., and R. V. Pisarev, Domain topography of antiferromagnetic $Cr_2O_3$ by second-harmonic generation, Appl. Phys. Lett. **66**, 2906 (1995).

[51] N. Hedrich, K. Wagner, O. V. Pylypovskyi, B. J. Shields, T. Kosub, D. D. Sheka, D. Makarov, and P. Maletinsky, Nanoscale mechanics of antiferromagnetic domain walls, arXiv:2009.08986.

[52] J. P. Tétienne, T. Hingant, L. J. Martinez, S. Rohart, A. Thiaville, L. H. Diez, K. Garcia, J. P. Adam, J. V. Kim, J. F. Roch, I. M. Miron, G. Gaudin, L. Vila, B. Ocker, D. Ravelosona, and V. Jacques, The nature of domain walls in ultrathin ferromagnets revealed by scanning nanomagnetometry, Nat. Commun. **6**, 6733 (2015).

[53] S. Vélez, J. Schaab, M. S. Wörnle, M. Müller, E. Gradauskaite, P. Welter, C. Gutgsell, C. Nistor, C. L. Degen, M. Trassin, M. Fiebig, and P. Gambardella, High-speed domain wall racetracks in a magnetic insulator, Nat. Commun. **10**, 4750 (2019).

[54] D. N. Astrov, N. B. Ermakov, A. S. Borovik-Romanov, E. G. Kolevatov, and V. I. Nizhankovskii, External quadrupole magnetic field of antiferromagnetic $Cr_2O_3$, J. Exp. Theor. Phys. Lett. **63**, 745 (1996).

[55] S. Mu and K. D. Belashchenko, Influence of strain and chemical substitution on the magnetic anisotropy of antiferromagnetic $Cr_2O_3$: An *ab-initio* study, Phys. Rev. Materials **3**, 034405 (2019).

[56] M. Fiebig, Nonlinear spectroscopy and topography on antiferromagnetic domains, Ph.D. thesis, Universität Dortmund, 1996.

[57] M. Fiebig, D. Fröhlich, B. B. Krichevtsov, and R. V. Pisarev, Second Harmonic Generation and Magnetic-Dipole-Electric-Dipole Interference in Antiferromagnetic $Cr_2O_3$, Phys. Rev. Lett. **73**, 2127 (1994).

[58] https://spin.ethz.ch/quantum-technology/nsdm.html, retrieved on 20 August 2020.

[59] A. Dréau, M. Lesik, L. Rondin, P. Spinicelli, O. Arcizet, J. F. Roch, and V. Jacques, Avoiding power broadening in optically detected magnetic resonance of single NV defects for enhanced dc magnetic field sensitivity, Phys. Rev. B **84**, 195204 (2011).

[60] R. Schirhagl, K. Chang, M. Loretz, and C. L. Degen, Nitrogen-vacancy centers in diamond: Nanoscale sensors for physics and biology, Annu. Rev. Phys. Chem. **65**, 83 (2014).

[61] K. D. Belashchenko, Equilibrium Magnetization at the Boundary of a Magnetoelectric Antiferromagnet, Phys. Rev. Lett. **105**, 147204 (2010).

[62] A. Andreev, Macroscopic magnetic fields of antiferromagnets, J. Exp. Theor. Phys. Lett. **63**, 758 (1996).

[63] Chromium sesquioxide ($Cr_2O_3$): Magnetic properties, in *Non-Tetrahedrally Bonded Binary Compounds II*, edited by O. Madelung, U. Rössler, and M. S. Schultz, Landolt-Börnstein - Group III Condensed Matter Vol. 41D (Springer-Verlag, Berlin, Heidelberg, 2000).

[64] I. A. Beardsley, Reconstruction of the magnetization in a thin film by a combination of Lorentz microscopy and external field measurements, IEEE Trans. Magn. **25**, 671 (1989).